### **RESEARCH PAPER**



# An autoadaptive Haar wavelet transform method for particle size analysis of sands

Andrea Ventola<sup>1</sup> • Roman D. Hryciw<sup>1</sup>

Received: 21 July 2022 / Accepted: 28 February 2023 / Published online: 8 May 2023 © The Author(s), under exclusive licence to Springer-Verlag GmbH Germany, part of Springer Nature 2023

#### **Abstract**

The Sed360 is a semi-automated image-based system for generating Particle Size Distributions (PSDs) of sands from an image of a sedimented soil specimen. The system expanded the size range of tested soils over its predecessors to include the entire range of sands, from 4.75 to 0.075 mm per the Unified Soil Classification System. In terms of exposed surface area, the largest particles are more than 4000 times larger than the smallest. This large size range posed a major challenge to image analysis. The solution, based on Haar Wavelet Analysis (HWT) was to autoadaptively adjust the sizes of HWT analysis squares: larger squares for parts of the image that contained larger particles, and progressively smaller squares working upward to the finest particles at the top of the sedimented soil column. From each analysis square, a single HWT index value, correlated to the size of the soil particles within the area, is determined. The particle sizes from across the entire image are combined to form the soil's PSD. The new autoadaptive analysis square sizing method was utilized on five sand specimens taken from the same parent material but with varying gradations, including finer and coarser sands, smaller and larger particle size ranges, and a challenging gap-graded material. The results showed strong agreement with results by sieving.

**Keywords** Image analysis · Particle size distribution · Sand · SedImaging · Sed360 · Soil classification

### 1 Introduction

A soil's particle size distribution (PSD) is an essential index property in geomechanics, geotechnical engineering, and related fields for classifying coarse-grained soils. The PSD, along with particle shape and relative density, also provide an initial estimate of soil properties such as compressibility, the angle of internal friction and soil unit weight [1–20]. The traditional method for determining a soil's PSD is through sieving, which, as Ohm et al. [15] discuss, is costly and energy- and time-intensive. Therefore, the use of image-based methods for determining PSDs has been expanding.

Andrea Ventola acvent@umich.edu

Roman D. Hryciw romanh@umich.edu

Department of Civil and Environmental Engineering, University of Michigan, 2350 Hayward Street, Ann Arbor, MI 48109, USA When soil particles settle through water, they naturally sort by size. The particles will deposit in an assembly with the coarsest grains at the bottom and progressively finer particles grading to the top. Ohm and Hryciw [14] showed that image analysis of such a sorted soil, following deposition through a laboratory column of water can produce the soil's particle size distribution (PSD). They referred to their system as "SedImaging" (short for sediment imaging).

Mathematical wavelet analysis has become a powerful tool in various civil engineering disciplines and related fields including tunneling [5], constitutive modeling of soils [13], structural dynamics [3], geophysics [16], seismology [21, 11], seismic exploration [2], site characterization [4], sedimentary geology [17], and soil particle characterization [19, 18]. Ohm and Hryciw [14] utilized wavelet analysis in their SedImaging system to generate PSDs for sands.

The image analysis developed by Ohm and Hryciw utilizes a Haar [6] Wavelet Transform (HWT) to produce hundreds of data points for the PSD. Each data point comes



from a small square section of the captured image. The "analysis squares" have hitherto been user-defined and of equal size, typically 128 pixel × 128 pixel. There are hundreds of such squares in a grid pattern covering the entire captured image. Since porosities in the sedimented soil column are relatively uniform [8] each analysis square represents the same volume percentage of the specimen's soil solids.

The HWT-based method does not determine the actual size of individual particles. Instead, it utilizes the image grayscale distribution to yield one data point representing the size of the particles in an analysis square. To work, the HWT method requires that an analysis square be *small enough* that the particles contained within it are approximately the same size. At the same time, the analysis square must be *large enough* so that it contains a statistically significant number of particles for the grayscale analysis.

Until now, the range of particle sizes that could be analyzed by SedImaging was limited to medium and fine sands (2.0 to 0.075 mm) per the Unified Soil Classification System. The percentage of fines can also be determined using a pre-washing technique [22]. This paper presents an advanced HWT technique, which more than doubles the range of particles that can be sized: up to 4.75 mm. Thus, PSDs covering the full range of coarse to fine sands (between US Standard sieves No. 4 and No. 200), can now be determined.

The expansion of the particle size range was made possible by new SedImaging hardware shown in Fig. 1. This

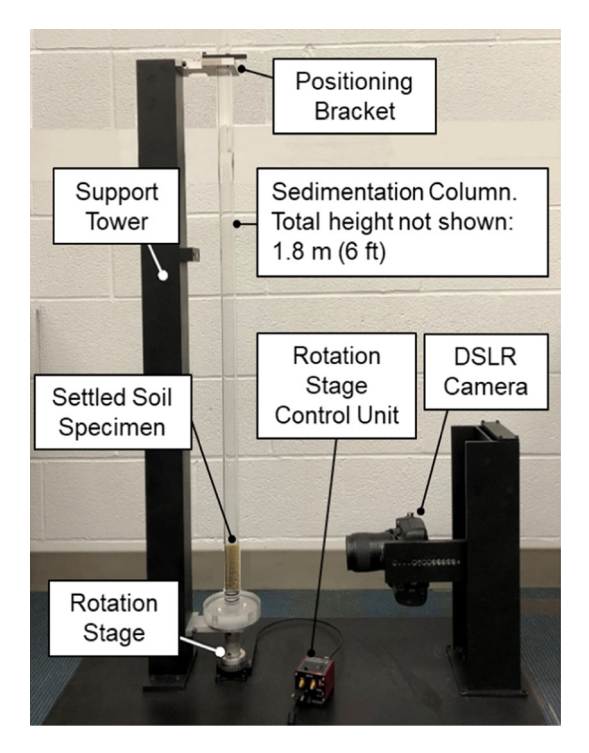


Fig. 1 The Sed360 hardware (adapted from Ventola and Hryciw [23])

new system is called the Sed360. Unlike its square-sectioned predecessors [14, 22, 24], the Sed360 uses a cylindrical sedimentation column with a 25.4 mm (1.0 in) diameter. After a soil specimen sediments through a 1.8 m (6 ft) water column and settles at the base as shown in Fig. 2a, the column is rotated on a precisely controlled circular stage. Images of the sorted soil are captured from a fixed camera location during rotation. Narrow vertical image strips are collected at 4° increments and stitched to form an "unwrapped image" of the specimen's surface as shown in Fig. 2b. The "unwrapped" image of a sorted specimen allows much larger particles to be analyzed than was possible with earlier SedImaging systems. Compete hardware details of the Sed360 and the procedure for stitching and analyzing the images is given in Ventola and Hryciw [23].

With the expanded testable particle size range afforded by the Sed360, the use of a fixed, user-defined analysis square for the HWT method is no longer viable. The square must adapt to the size of the particles within it. This paper shows why this is necessary and presents an autoadaptive approach that tailors analysis squares' size to the size of the particles within them.

### 1.1 The Haar wavelet transform (HWT) analysis for sedimaging

To understand the need for variable HWT analysis squares, a short introduction to the Haar Wavelet Transform, as it is

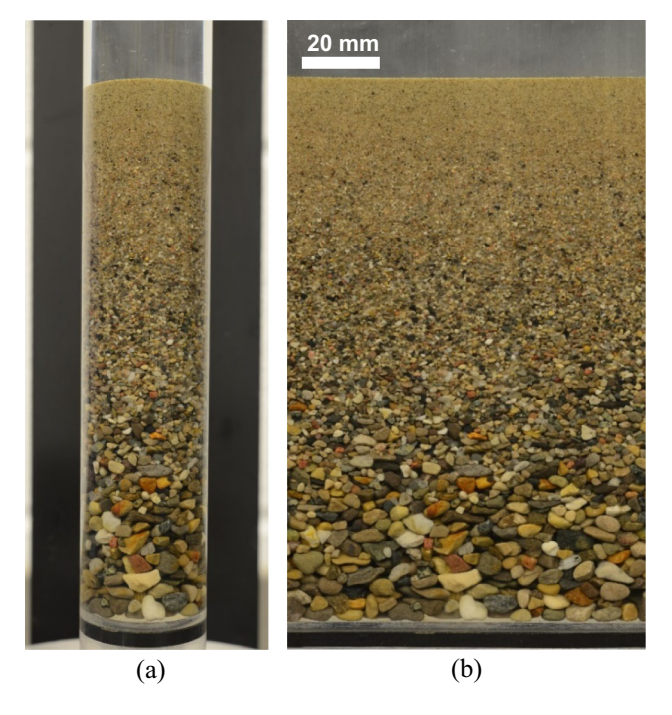


**Fig. 2** Soil specimen in the Sed360. **a** Image captured during sedimentation column rotation, **b** Unwrapped view of the soil specimen perimeter



used with SedImaging, is useful. A formal mathematical description was given by Hryciw et al. [7] and interested readers are encouraged to refer to it. Nievergelt [12] provides a broader explanation of wavelet mathematics. Here, a less rigorous description, sufficient for this paper's needs, is presented.

For the HWT, an analysis square must be  $2^n \times 2^n \operatorname{pix}^2$  in size where n has, until now, typically been seven (i.e.  $2^7 = 128 \operatorname{pixels}$ ). Since sedimentation through water sorts a soil specimen by particle size, each of the HWT analysis squares contains particles of approximately the same size. As mentioned previously, relative uniformity of particle sizes within each analysis square is critical to the analysis. Figure 3 shows the grayscale version of the soil from Fig. 2. Overlaying the image is a grid of  $256 \times 256 \operatorname{pix}^2$  analysis squares. It is easy to see that the grid is too fine for the largest particles at the bottom. It is less obvious that the grid is too coarse for the smallest particles at the top, but this will be demonstrated in Sect. 2.2.

For each and every one of the analysis squares in Fig. 3, such as the single one shown in Fig. 4, an "Energy" (E) is computed at n "decomposition levels" (DL). At the first DL,  $E_1$  reflects the magnitude of the difference in grayscale values of adjacent pixels throughout the analysis square. The Energy at the second DL,  $E_2$ , reflects the difference between average grayscale values of adjacent  $2 \times 2$  pix<sup>2</sup>

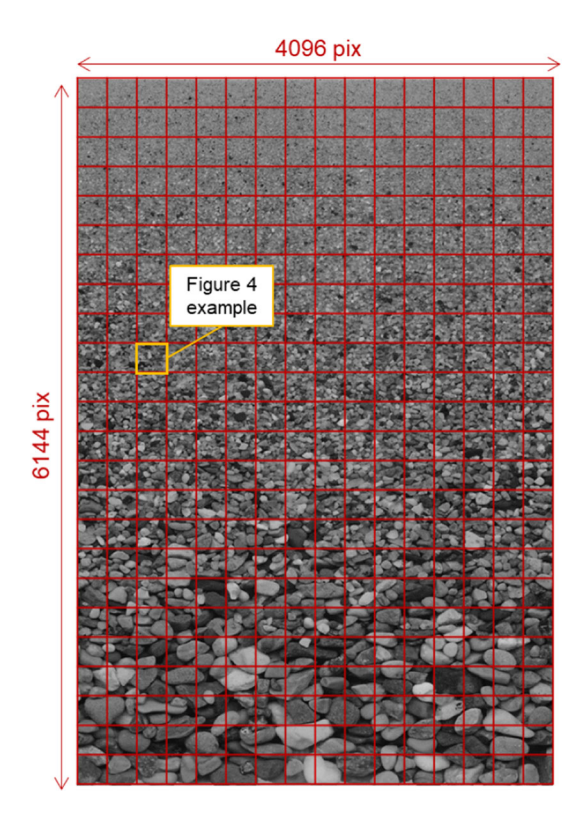


Fig. 3 Sample soil specimen from Fig. 2 with an overlaid grid of  $256 \times 256 \ \text{pix}^2$ 

areas throughout the analysis square. At the third DL,  $E_3$  is a measure of the difference of average grayscale values between adjacent  $4 \times 4 \text{ pix}^2$  areas, and so on. The greater the difference in averaged grayscale values between compared areas, the larger the E. Regardless of n, at the final decomposition level,  $E_n$  quantifies the difference in average grayscale values between the four quadrants of the analysis square.

Many sands are composed of multicolored grains, or at least different shades of the same color. The important benefit of this is that an analysis area's E will be largest at the DL at which the pixel area of "grayscale averaging" approximately coincides with the size of the soil particles within the analysis square. This point is illustrated in Fig. 4, which shows the distribution of E by DL (Fig. 4a) for the example analysis square called out in Fig. 3. Also shown in Fig. 4 are the grids corresponding to the grayscale averaging areas at the 5th  $(16 \times 16 \text{ pix}^2)$ , 6th  $(32 \times 32 \text{ pix}^2)$ , and 7th  $(64 \times 64 \text{ pix}^2)$  DLs. To the right of each of the three gridded analysis squares, pixel values have been replaced with each area's average grayscale. As compared to the 5th and 7th DLs, the differences in average grayscale values of adjacent grid areas is more pronounced at the 6th DL. Thus, the E is greatest around the 6th DL. By visual observation of Fig. 4, the particle size is best approximated by the size of the grid at the 6th level, where E is largest.

At a fixed image magnification, Energy distributions shift to the right (to higher *DLs*) with increasing particle size. Shin and Hryciw [18] observed that the centroid of the area (*CA*) under the *E* vs. *DL* plot correlated very well with the size of particles in the analysis square (where particle size is defined by sieve opening). The *CA* for the example analysis square in Fig. 4 is 5.07. A calibration curve between *CA* and the *Pixels per Particle Diameter (PPD)* was established by Hryciw et al. [9]. This calibration curve is plotted in Fig. 5 and given by the equation:

$$PPD = \left(\frac{CA}{2.4}\right)^{5.1} \tag{1}$$

The HWT analysis is performed for all of the analysis squares (in Fig. 3), the *CA* values are computed for each square, and the corresponding *PPD*s are found by Eq. 1. The *PPD* values are then converted to actual particle sizes using the known image magnification in units of pixels/mm. The particle sizes are ranked from largest to smallest and plotted as the soil's PSD.



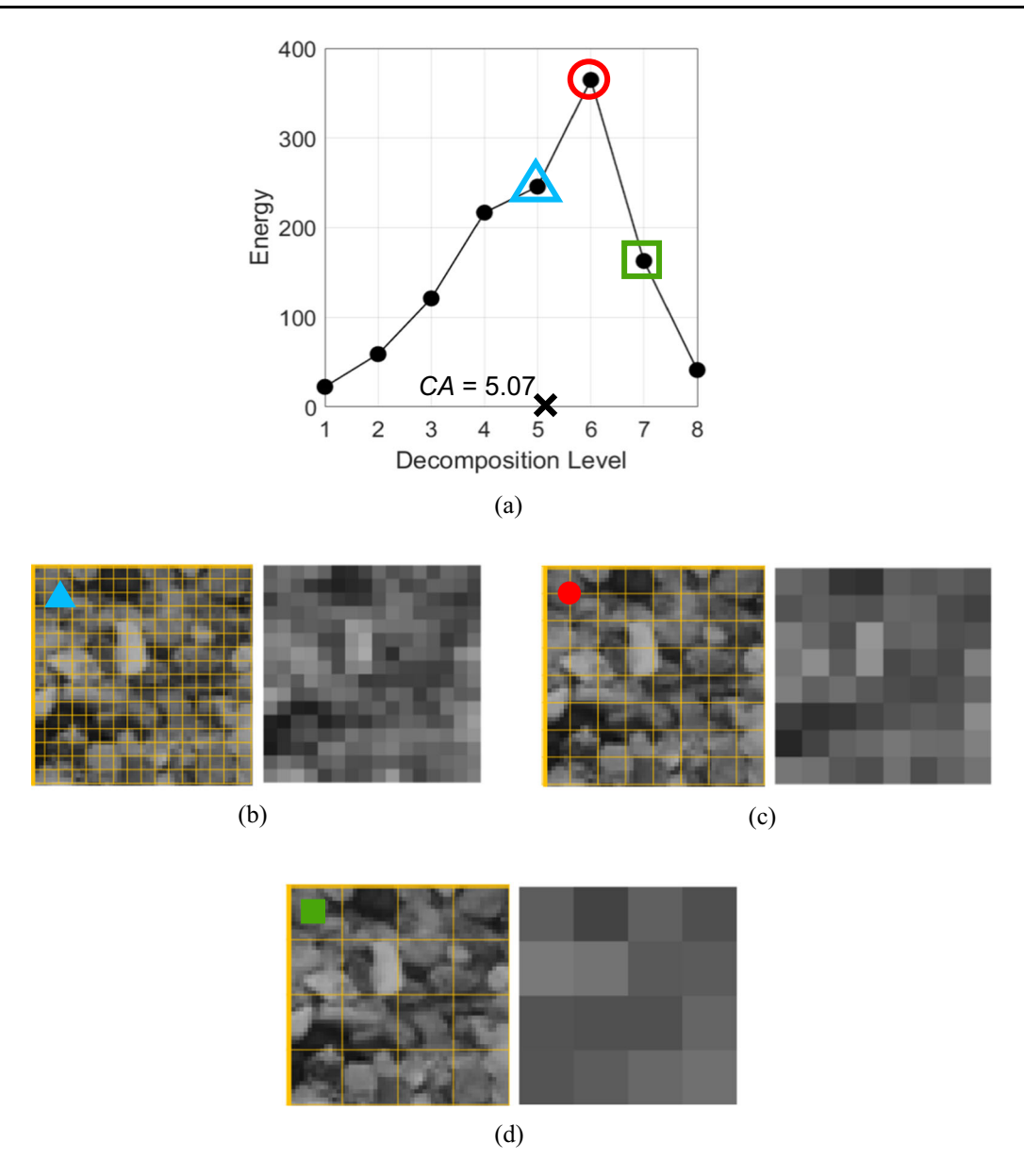


Fig. 4 Example of the HWT method used with SedImaging. a Energy versus decomposition level, b grayscale averaging areas for the 5th, c 6th, and d 7th decomposition levels

### 2 Motivation

With the expanded range of testable soil particle sizes afforded by the new Sed360, the accuracy of the existing HWT-based analysis method required reexamination. Two significant issues were revealed: (1) The existing *PPD-CA* calibration (Eq. 1) required an update, and (2) Using a fixed HWT analysis area size (regardless of the area's pixel dimensions) to evaluate an entire non-uniform soil specimen yields inaccurate PSDs. These two issues motivated development of the new, autoadaptive HWT image analysis approach described herein.

### 2.1 The new PPD-CA calibration

The original *PPD-CA* calibration (Eq. 1) was developed using older camera technology and a narrower particle size range. *PPD* values ranged only between 2 and 60. With new Sed360 hardware and the expanded particle size range, *PPD*s can now range to above 200. This warranted an investigation into how well Eq. 1 fits data at these much higher *PPD*s. To perform this recalibration, sand particles were sieved into 11 narrow size ranges as listed in Table 1. The sand is a glacio-fluvial material referred to as "2NS" by the Michigan Department of Transportation [10].



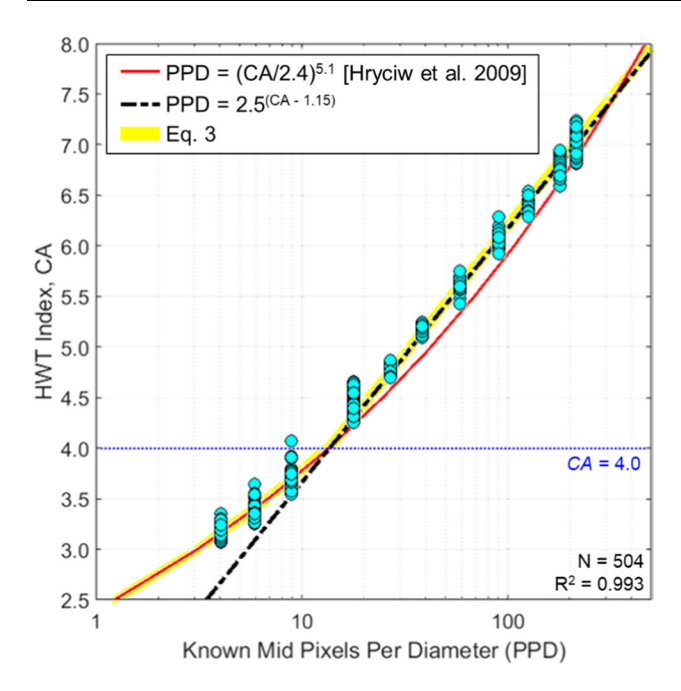


Fig. 5 PPD-CA calibration using the Sed360 data from Table 1

The *CA* values for the 504 analysis squares listed in Table 1 were determined and are plotted versus the corresponding mid-*PPD* values in Fig. 5. Equation 1 (solid red line) remains a good fit for *PPD*s of 4.1, 5.9, and 8.9. However, at higher *PPD*s, the calibration points are better fitted by:

$$PPD = 2.5^{(CA-1.15)} (2)$$

Equation 2 is a straight line in the semi-log scale of Fig. 5. This equation was obtained by fitting the data above PPD = 15 to maximize the coefficient of determination,  $R^2$ . Hryciw et al. [7] anticipated that when camera technology advances to higher resolutions, the PPD-CA

calibration would be linear of the form given by Eq. 2. At the same time, there is good reason for the flattening of the curve below  $PPD \approx 15$ . When PPDs are low, the E values are high at low DLs. Because there is no data below DL = 1, the "E curves" are truncated at the 1<sup>st</sup> decomposition level. This results in an increasing compression of CA values as PPD moves downward from about 15 (i.e.  $CA \approx 4$ ).

Ideally, a single equation would fit the entire PPD range, but at the present time, this would require a drastic change to image acquisition. Camera magnifications would have to be increased so that PPDs are always greater than 15. In other words, the finest (0.075 mm) sand particles would require PPD = 15. This in turn would require a camera magnification of 200 pixels/mm (about four times the current magnification). Unfortunately, this would decrease the camera's field of view so much that several photos in the vertical direction would be needed, possibly at different camera magnifications, to photograph the entire soil specimen. Such complexity would make Sed360 testing cumbersome. Therefore, to maintain simplicity of the Sed360 hardware (as well as the analysis) the authors recommend using the following piece-wise PPD-CA calibration:

$$PPD = \begin{cases} \left(\frac{CA}{2.4}\right)^{5.1} (Eq.1) \text{ if } CA \le 4.0\\ 2.5^{(CA-1.15)} (Eq.2) \text{ if } CA > 4.0 \end{cases}$$
 (3)

Equation 3 is highlighted in yellow in Fig. 5. The R<sup>2</sup> value of Eq. 3 for the calibration data is 0.993. Equation 3 is used for obtaining all of the HWT-based PSD results presented in this paper.

Table 1 2NS sand ranges for Sed360 calibration testing

Size range no.	Sieve range	Size range [mm]	Corresponding <i>PPD</i> range <sup>a</sup>	Mid PPD	Number of analysis squares (i.e. data points in Fig. 5)			
1	No. 4 to No. 5	4.75–4.00	233.2–196.4	214.8	42			
2	No. 5 to No. 6	4.00-3.35	196.4–164.5	180.5	46			
3	No. 7 to No. 8	2.80-2.36	137.5-115.9	126.7	45			
4	No. 10 to No. 12	2.00-1.70	98.2-83.5	90.8	35			
5	No. 14 to No. 18	1.40-1.00	68.7-49.1	58.9	28			
6	No. 20 to No. 25	0.85-0.71	41.7–34.9	38.3	30			
7	No. 30 to No. 35	0.60-0.50	29.5-24.6	27.0	22			
8	No. 40 to No. 50	0.425-0.300	20.9-14.7	17.8	72			
9	No. 70 to No. 100	0.212-0.150	10.4-7.4	8.9	66			
10	No. 100 to No. 170	0.150-0.090	7.4–4.4	5.9	80			
11	No. 170 to No. 200	0.090-0.075	4.4–3.7	4.1	38			
					$\Sigma$ 504			

<sup>&</sup>lt;sup>a</sup>Image magnification = 49.1 pix/mm



### 2.2 Impact of different-sized HWT analysis squares

While the establishment of Eq. 3 is crucial to accurately characterize the expanded particle size range in the Sed360, the greater improvement (and the main focus of this paper) stems from the need for autoadaptive determination of the HWT analysis square sizes. To illustrate this need, Fig. 6 presents the PSDs for the sand shown in Figs. 2 and 3. This image was analyzed using the HWT-based method four separate times. Each time, a single analysis square size was used for the entire image. Sieving results following ASTM C136/C136M-19 [1] are also shown.

Figure 6 reveals that none of the four PSDs using unisized analysis squares matches the full range of sieve-based results. Only the PSD using  $1024 \times 1024$  pix<sup>2</sup> analysis

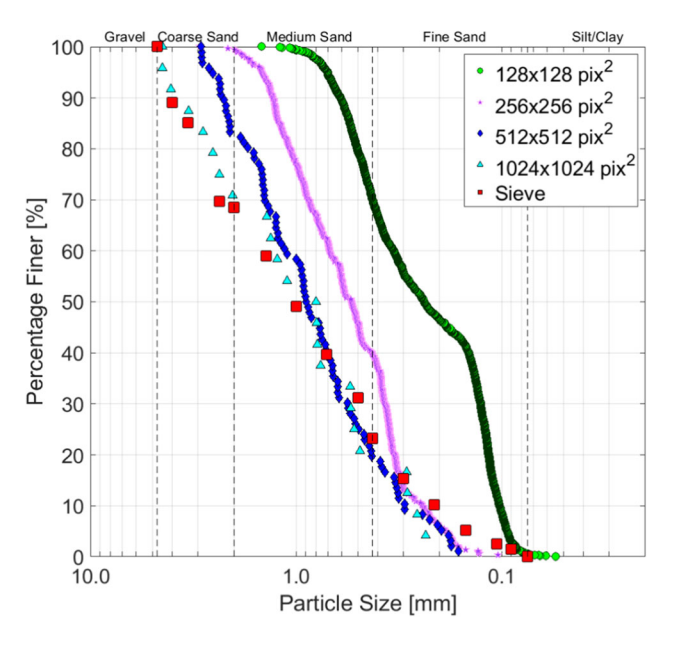
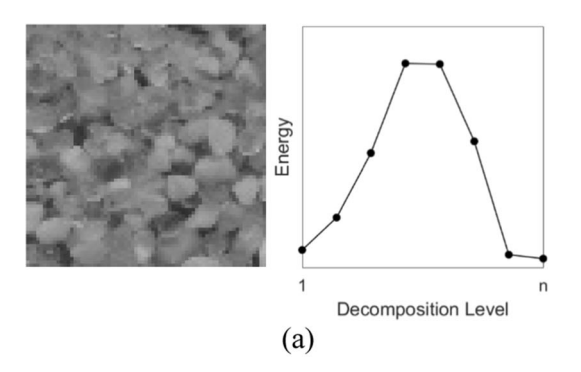


Fig. 6 PSD results for the same sand specimen image using different sizes of HWT analysis squares



squares correctly sizes the coarse sand. Conversely, only the  $128 \times 128 \text{ pix}^2$  analysis squares correctly size the finest sand. Figure 6 confirms that variable size windows are needed to correctly characterize specimens containing particles over the full spectrum of sand sizes; larger squares should be used for coarser sand, and smaller squares for finer sand. In response to these findings, a procedure was developed to autoadaptively select the sizes of the analysis squares to suit the various particle sizes.

# 3 Autoadaptive sizing of analysis squares: energy distributions

The great majority of E-distributions follow a pattern as shown in (Figs. 4 and 7). These ideal distributions display low E at low DLs, gradually rise with increasing DL, then steepen and peak at a midrange DL. The E then monotonically decreases back to low levels at the highest DLs. When a distribution follows this quasi-parabolic pattern, particle sizes determined by Eq. (3) will be accurate and reliable. We therefore refer to E-distributions such as those in Figs. 4 and 7 as "acceptable".

On occasion, an *E*-distribution does not follow an acceptable pattern. In such cases, Eq. (3) does not yield an accurate *PPD*. Figure 8 shows examples of such undesirable *E*-distributions. In Fig. 8a the analysis square is too small for the particle size and thus, the *E*-distribution fails to decrease at high *DLs*. This truncation of the *E*-distribution results in an inappropriately low computed *CA* value and underestimation of *PPD* by Eq. (3). A similar, although less pronounced underestimation of *CA* can also occur for an *E*-distribution that peaks at the second largest (*n*-1) *DL*. In this case (not shown in Fig. 8), the analysis square is still too small, and should not be used.

The analysis square in Fig. 8b is too large because it contains particles with a wide range of sizes. Larger sand particles are at the bottom of the square, with progressively finer sand above. The corresponding *E*-distribution peaks

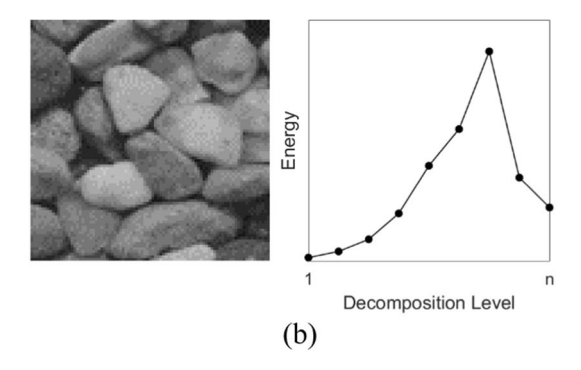
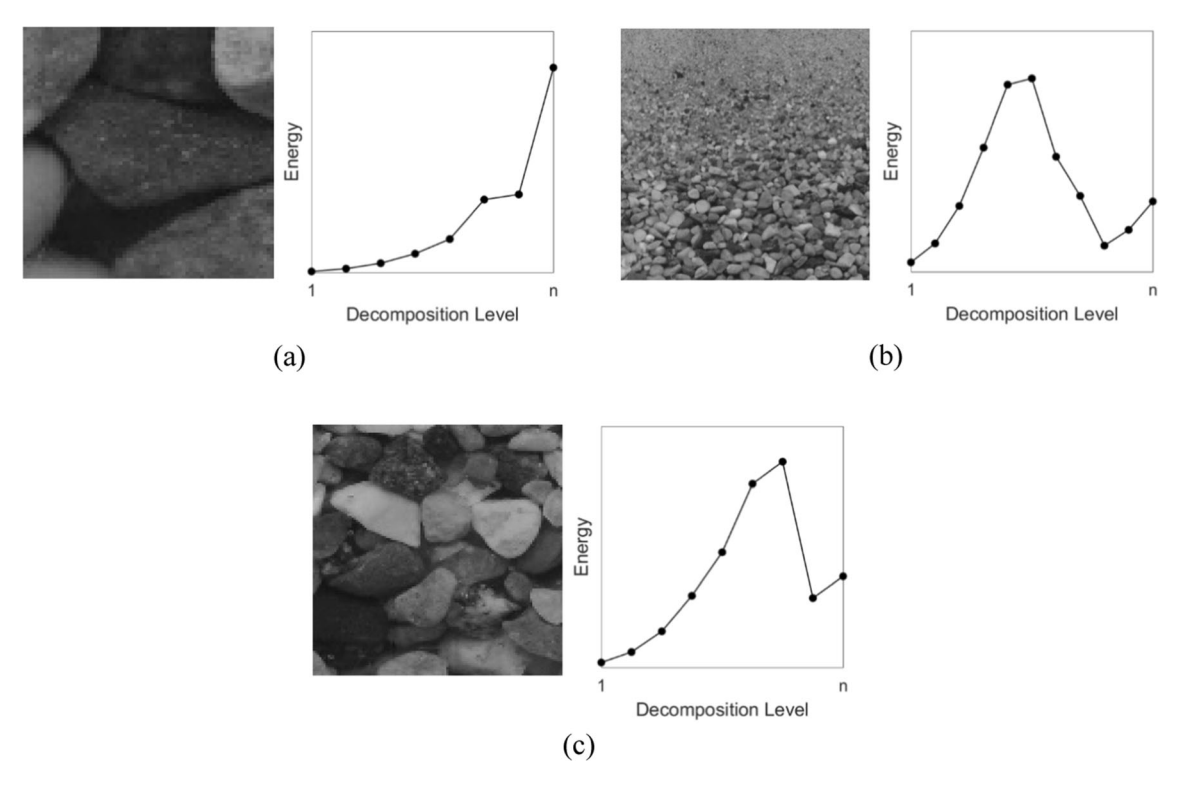


Fig. 7 Examples of analysis squares with "acceptable" *E*-distributions. **a** analysis square containing smaller particles, and **b** square containing larger particles





**Fig. 8** Examples of analysis squares with "unacceptable" *E*-distributions. **a** HWT analysis square is too small relative to the soil particles, **b** range of particle sizes is too large and **c** energy curve impacted by particle coloring

around DL = 5 to 6 before decreasing. However because of the wide range of soil particle sizes in the analysis square, the energy distribution begins to increase again at DL = n-1 and n. The reason for this E increase is that at DL = n-1 and n, large areas of averaged grayscale values are being compared to other large areas of averaged grayscales.

When particles of greatly different sizes are contained within compared areas, the averaged grayscale values can differ enough to cause the increases in E at these higher DLs.

Another example of unusual features impacting the *E*-distribution is shown in Fig. 8c. Like the *E*-distribution in Fig. 8b, the one in Fig. 8c also increases at the final decomposition level, *n*. Here, the *E* increase is caused by the proximity of similarly colored particles. Three large light-colored particles in Fig. 8c occupy almost 50% of the top half of this analysis square. Moreover, the bottom left quadrant of Fig. 8c contains a very dark particle. Because of the large areas of high contrasting grayscale values and their location within the analysis square, the *E* at the final *DL* jumps up. This upturn in *E* at the last *DL* shifts *CA* to the right and causes an overestimation of particle size.

It is important to emphasize that while the E-distributions in Fig. 8b and c are both "unacceptable", the causes of the undesirable increasing E at the highest DLs are different. In Fig. 8b, the analysis square contains a range of particle sizes that is too large. Conversely, the size of the

analysis square in Fig. 8c is actually "acceptable"; it contains particles of about the same size (i.e. the square is not too big) and it also contains enough soil particles (i.e. the square is sufficiently large). Instead, the "unacceptability" regarding Fig. 8c is due to the happenstance proximity of certain-colored soil particles. While Fig. 8b and c have similarly shaped "unacceptable" *E*-distributions, the autoadaptive analysis square sizing method will use different procedures for addressing these two situations.

# 4 The autoadaptive sizing of analysis squares

### 4.1 Basic principles

The autoadaptive analysis square sizing is predicated on four principles:

(a) It is a reasonable assumption that soil particles of the same size are located at the same elevation of a sorted Sed360 specimen. Therefore, the *E*-distributions of all analysis squares at the common elevation are collectively used for the selection of the analysis area size. The same square size is then assigned for a given elevation across the entire width of the image.



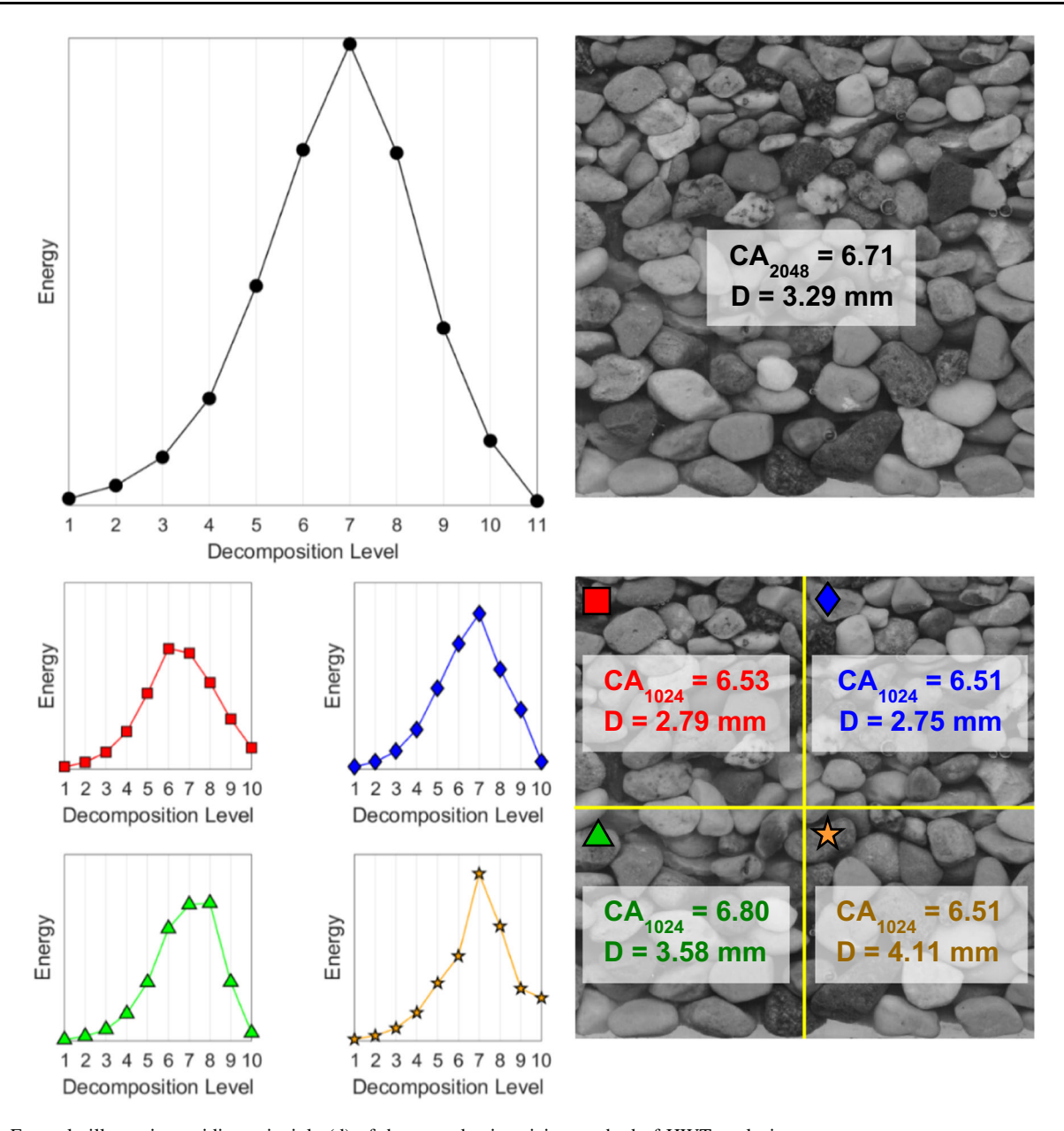


Fig. 9 Example illustrating guiding principle (d) of the autoadaptive sizing method of HWT analysis squares

- (b) The distinctions between "acceptable" and "unacceptable" E-distributions discussed with Figs. 7 and 8 are utilized by the autoadaptive procedure. Acceptable E-distributions are used "as is" while unacceptable distributions are used after being adjusted. The adjustment procedure is discussed in Sect. 4.2.
- (c) Larger analysis squares are preferred for larger particle sizes because larger analysis squares can be decomposed to more (higher) levels, and thus, the E-distribution is less likely to be truncated at DL = n. With less truncation, the computed CA will yield a more reliable PPD by Eq. (3).
- (d) Despite the preference for larger analysis squares as noted in the third principle, the smallest "acceptable" analysis squares are used for better resolution of particle sizes. Even if a larger analysis square yields an "acceptable" E-distribution, the E-distributions of the contained smaller analysis areas are investigated for acceptability before final selection of an analysis square size.

Figure 9 illustrates principle (d). Here, a  $2048 \times 2048$  pix<sup>2</sup> analysis area contains coarse sand particles. Based on the discussion of "acceptable" *E*-distributions in Fig. 7, the *E*-distribution for this large  $2048 \times 2048$  pix<sup>2</sup> area is "acceptable". It exhibits a peak at one of the mid-range



DLs and E is low at the upper levels. Using Eq. 3 and a known camera magnification, the size of this area's particles is found to be D = 3.29 mm. When the square is quartered, the  $1024 \times 1024$  pix<sup>2</sup> areas reveal four E-distributions that are also "acceptable". The top two  $1024 \times 1024 \text{ pix}^2$  areas yield particle sizes of 2.79 and 2.75 mm which, as expected, are smaller than the one determined for the entire  $2048 \times 2048 \text{ pix}^2$  area. The bottom two  $1024 \times 1024$  pix<sup>2</sup> areas yield larger particle sizes of 3.58 and 4.11 mm. The size difference between particles in the top and bottom halves of the  $2048 \times 2048$ pix<sup>2</sup> area is visible by eye in Fig. 9. In summary, while the  $2048 \times 2048 \text{ pix}^2$  analysis area's E-distribution was "acceptable", using the smaller (and also acceptable)  $1024 \times 1024$  pix<sup>2</sup> areas leads to more accurate particle sizes.

#### 4.2 Procedure

After a soil specimen is sedimented, photographed, and "unwrapped", it is ready for the autoadaptive analysis window sizing by the following procedure:

- (1) The entire soil specimen is discretized into  $2048 \times 2048 \text{ pix}^2$ , then  $1024 \times 1024 \text{ pix}^2$ ,  $512 \times 512 \text{ pix}^2$ ,  $256 \times 256 \text{ pix}^2$ , and finally,  $128 \times 128 \text{ pix}^2 \text{ HWT}$  analysis squares.
- (2) The *E*-distributions are computed for all of the analysis squares. When the *E*-distribution takes an upward turn at high *DL*s, the high *E* values are automatically set to zero by the computer code. This same zeroing of *E* at high *DL*s was performed during the calibration that produced Eq. (3).
- (3) Selection of the appropriate size of analysis squares by the code is automatically determined using the flow chart in Fig. 10. The investigation begins with the largest analysis square size of 2048 × 2048 pix<sup>2</sup>. Analysis starts with the lowest row of 2048 × 2048 pix<sup>2</sup> analysis squares in the image and progresses upward. With each new 2048 × 2048 pix<sup>2</sup> row, Fig. 10 is used from "Start". The smallest allowable analysis square size anywhere in the image is set at 128 × 128 pix<sup>2</sup>.
- (4) Using the appropriate analysis square sizes determined by Fig. 10, the CA values for all of the areas are computed. Equation (3) converts the CA values to PPD, and with the known camera magnification, the actual particle size representing the analysis square is computed.
- (5) Since analysis squares have varying sizes, the particle sizes are weighted by the size of the analysis squares when developing the PSD.

### **5 Results**

Five soil specimens were tested in the Sed360 using the autoadaptive analysis square sizing method. The stitched "unwrapped" views of these specimens are in Fig. 11. The specimens contain varying amounts of coarse (4.75 to 2 mm), medium (2 to 0.425 mm), and fine sand (0.425 to 0.075 mm). The exception is Specimen B, which contains only coarse and fine sand. The same 2NS parent soil was used for all five engineered specimens so that the study would focus only on the performance of the autoadaptive method on different size gradations, rather than on different soil types. For comparison of the HWT image-based method to sieving results for other soils, readers are referred to Ohm and Hryciw [14], Ventola and Hryciw [24], Ventola et al. [22], and Ventola and Hryciw [23].

Figures 12, 13, 14, 15, and 16 show the grayscale images of the five specimens. Overlaying each of these images is a grid showing the analysis squares autoadaptively selected by the code. All five specimens required analysis squares ranging from  $128 \times 128$  pix<sup>2</sup> to  $1024 \times 1024 \text{ pix}^2$ . Although  $2048 \times 2048 \text{ pix}^2$  areas were the starting point in all five cases, no such large analysis area was found to be appropriate. The resulting PSDs are also plotted in Figs. 12, 13, 14, 15, and 16 with comparisons to sieving results. Table 2 summaries the PSDderived parameters ( $D_{60}$ ,  $C_u$  etc.). To emphasize the benefit of the autoadaptive method, Table 2 also lists the PSD parameters obtained by using the older approach of unisized analysis squares, in this case, only  $256 \times 256 \text{ pix}^2$ . The  $256 \times 256$  pix<sup>2</sup> results are clearly inferior to the autoadaptive results and therefore, are not plotted in Figs. 12, 13, 14, 15, and 16 and will not be further discussed.

### 6 Analysis of results

As seen in Figs. 12, 13, 14, 15, and 16, for all five of the sand specimens, the coarsest sand particles that were first to settle at the base of the sedimentation column require larger HWT analysis squares; as finer sand particles settle overtop larger ones, progressively smaller analysis squares were automatically adopted. Because of the different window sizes, the coarser portions of the sands' Sed360 PSDs contain fewer data points while the finer sand portions of the PSDs have more points. Naturally, for the specimens with greater percentages of coarse sand (Specimens A, B, and C), more of the larger ( $1024 \times 1024 \text{ pix}^2$  and  $512 \times 512 \text{ pix}^2$ ) analysis squares were employed than for the specimens with more fine sand (Specimens D and E). These trends are visualized in the stacked bar graphs in



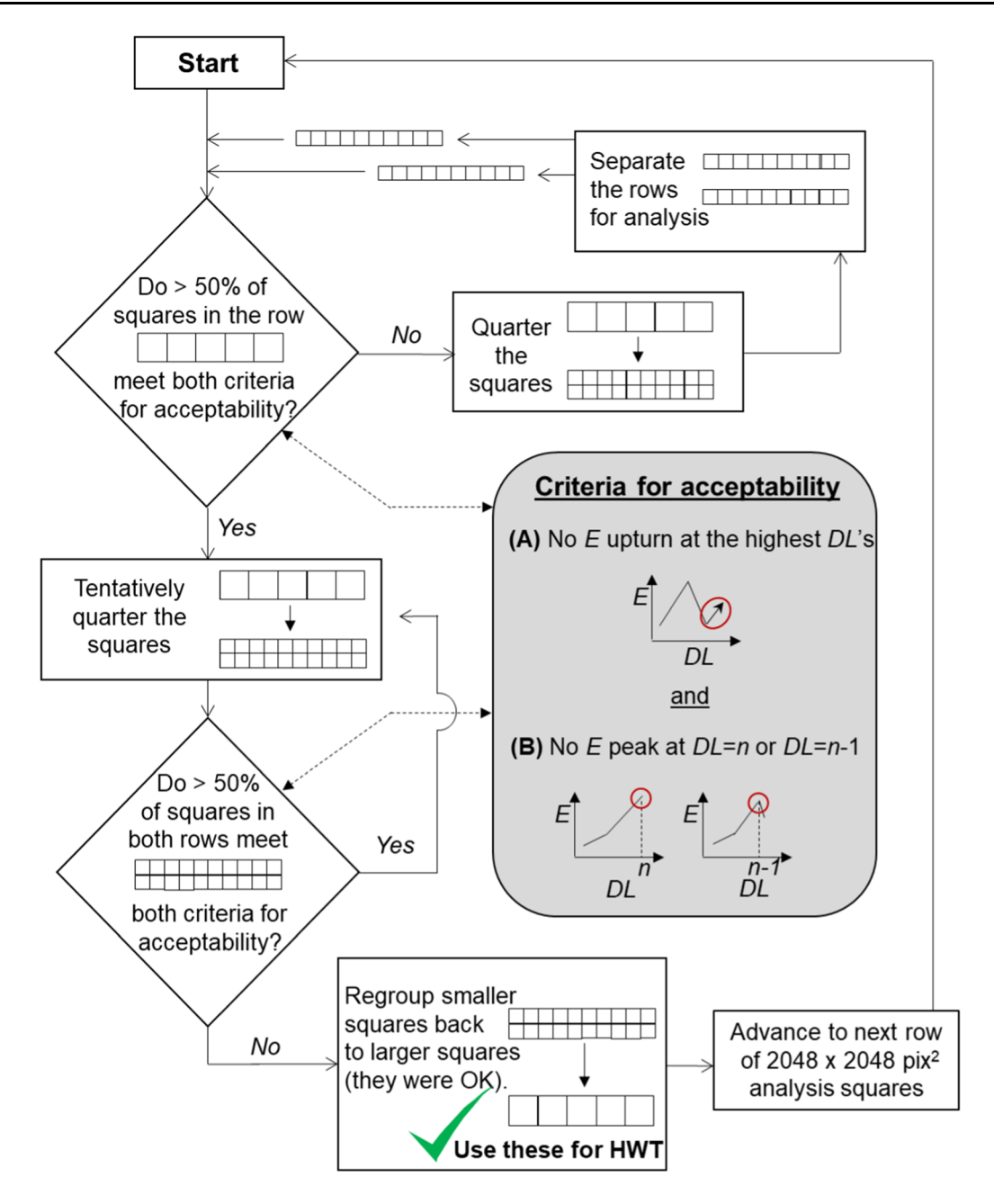


Fig. 10 Flow chart followed in Step 3 of the autoadaptive HWT analysis square sizing method

Fig. 17. About 50% of Specimens B and E are fine sand, which is reflected in the high number of the smallest analysis square ( $128 \times 128 \text{ pix}^2$ ) being employed for these two specimens.

The gap-graded Specimen B (Fig. 13a) illustrates an important success of the autoadaptive method. Specimens A, C, D, and E have a continuous and uninterrupted flow of larger HWT analysis squares from the bottom of the images to progressively smaller squares moving up the image. By contrast, in the middle of Specimen B near the interface between coarse and fine sand,  $512 \times 512$  pix<sup>2</sup> analysis squares were adopted. Above them there is an immediate

jump to  $128 \times 128$  pix<sup>2</sup> squares. This is a logical and expected result for a gap-graded sand. More interestingly, above the row of smaller squares, larger  $256 \times 256$  pix<sup>2</sup> squares were selected by the autoadaptive procedure. Here, the small sand particles dictate the use of the smallest squares ( $128 \times 128$  pix<sup>2</sup>), but various locations of different particle colors necessitated two rows of larger squares ( $256 \times 256$  pix<sup>2</sup>) above the two rows of smaller squares. To elaborate on this observation, had smaller analysis squares been used in this region, clustered black particles within the lighter colored sand could lead to undesired upturns in *E*-distributions at the highest decomposition



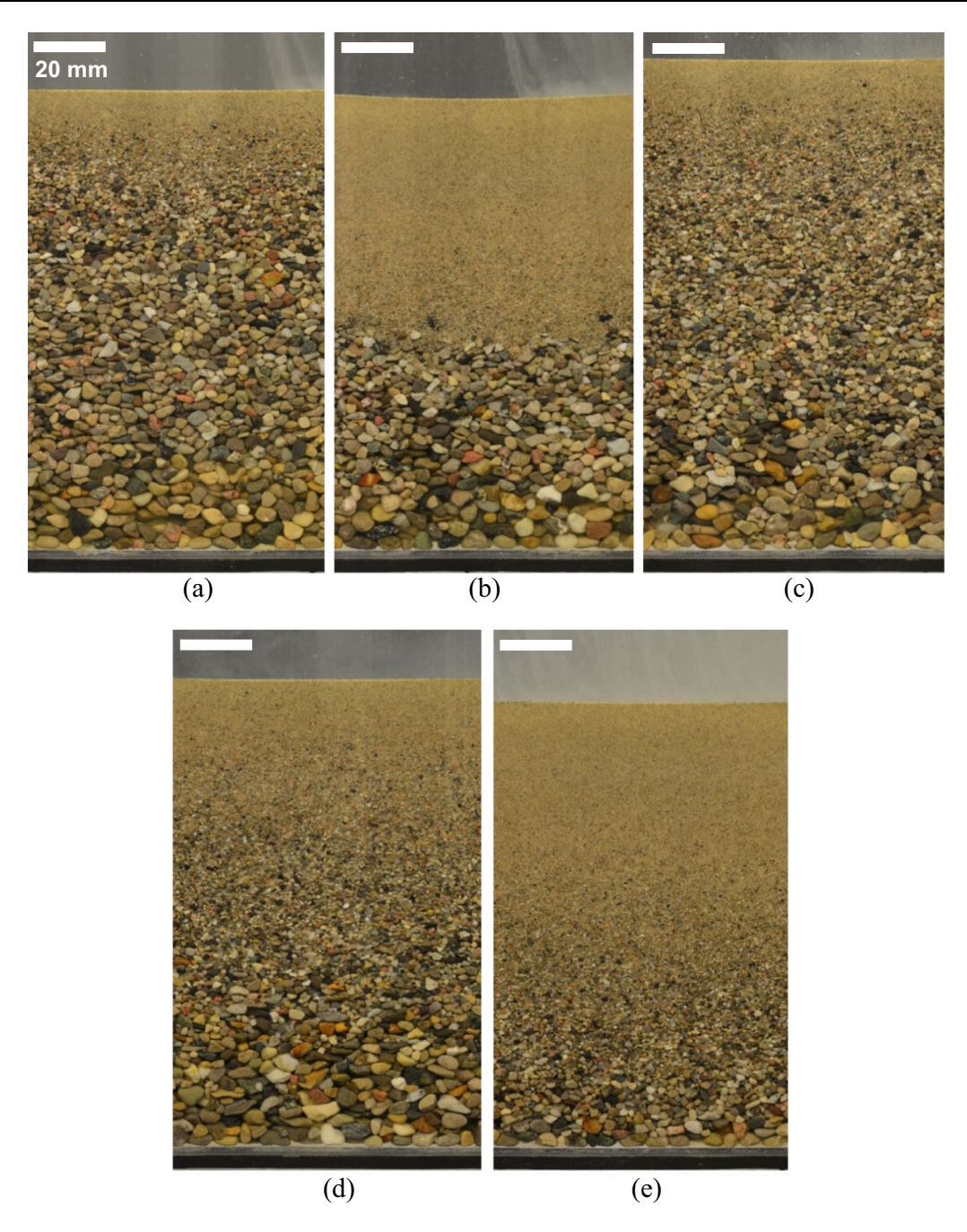


Fig. 11 Specimens tested having the following size percentages per sieve analysis (coarse/medium/fine): a 67/23/10, b 50/0/50, c 37/51/12, d 31/46/23, and e 10/40/50

levels. The autoadaptive procedure eliminates this problem by effectively "diluting" the local effects over larger  $256 \times 256 \ \text{pix}^2$  areas. The topic of gap-graded sands will be visited again in a separate discussion in Sect. 6.2.

### 6.1 Comparison of Sed360 and sieving results

Overall there is very good agreement between the autoadaptive Sed360 PSD and the sieving results for all five sand specimens. In all five cases, the percentages of

fine sand by the autoadaptive method and by sieving (see Table 2) are virtually identical. This excellent agreement is also seen in Figs. 12, 13, 14, 15, and 16 where at 0.425 mm, the Sed360 and sieving curves coincide. However, at the tail end of the curves, the autoadaptive Sed360 typically undersizes the smallest particles. This could be due to small errors in the manual cropping of Sed360 images. Or, ambient light may be illuminating the tops of the soil specimens, thus making the top row of analysis areas appear to contain larger particles than are actually



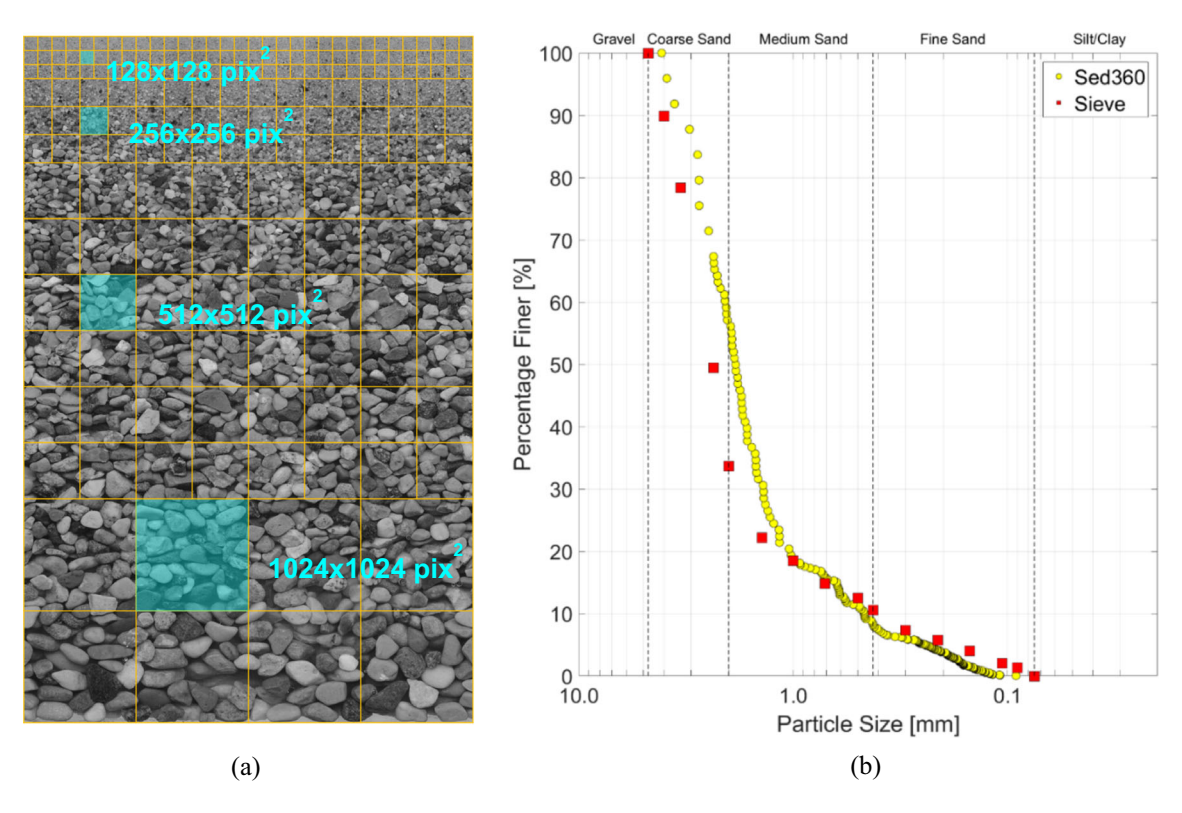


Fig. 12 Sed360 Results for Specimen A. a Autoadaptively determined analysis squares used to generate the HWT-based PSD, b PSD results

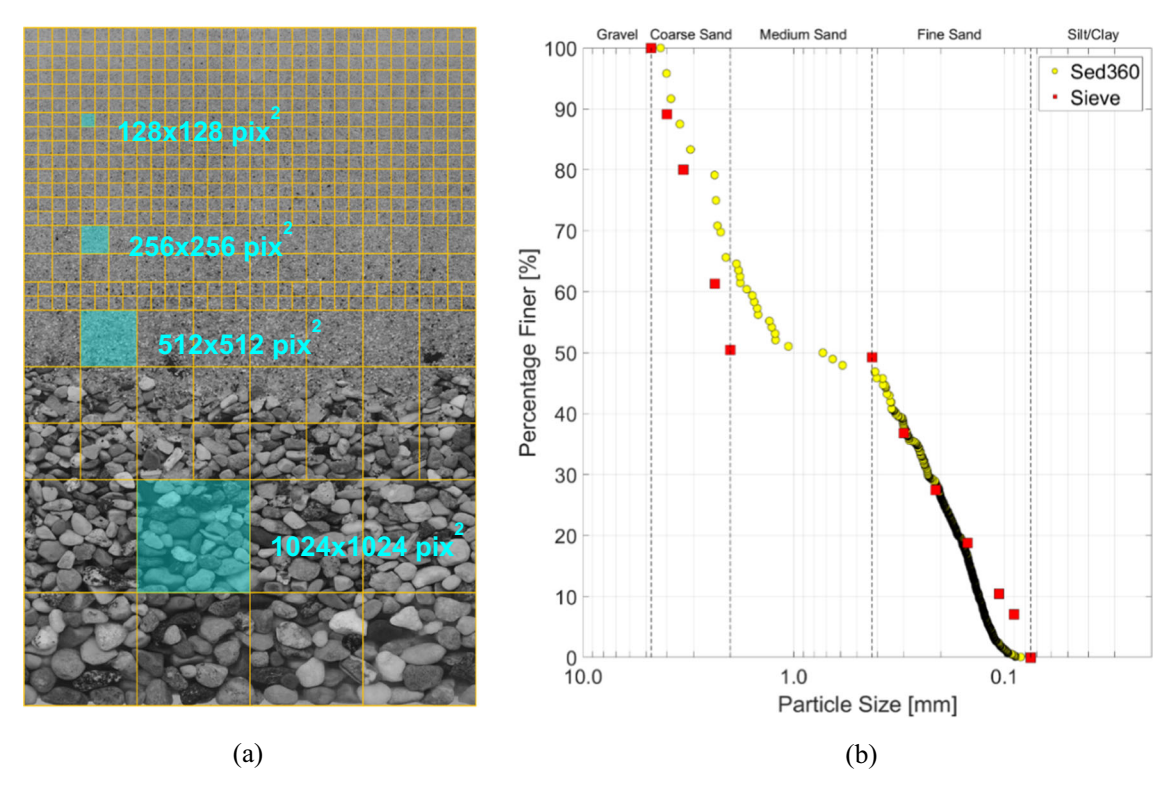


Fig. 13 Sed360 Results for Specimen B. a Autoadaptively determined analysis squares used to generate the HWT-based PSD, b PSD results



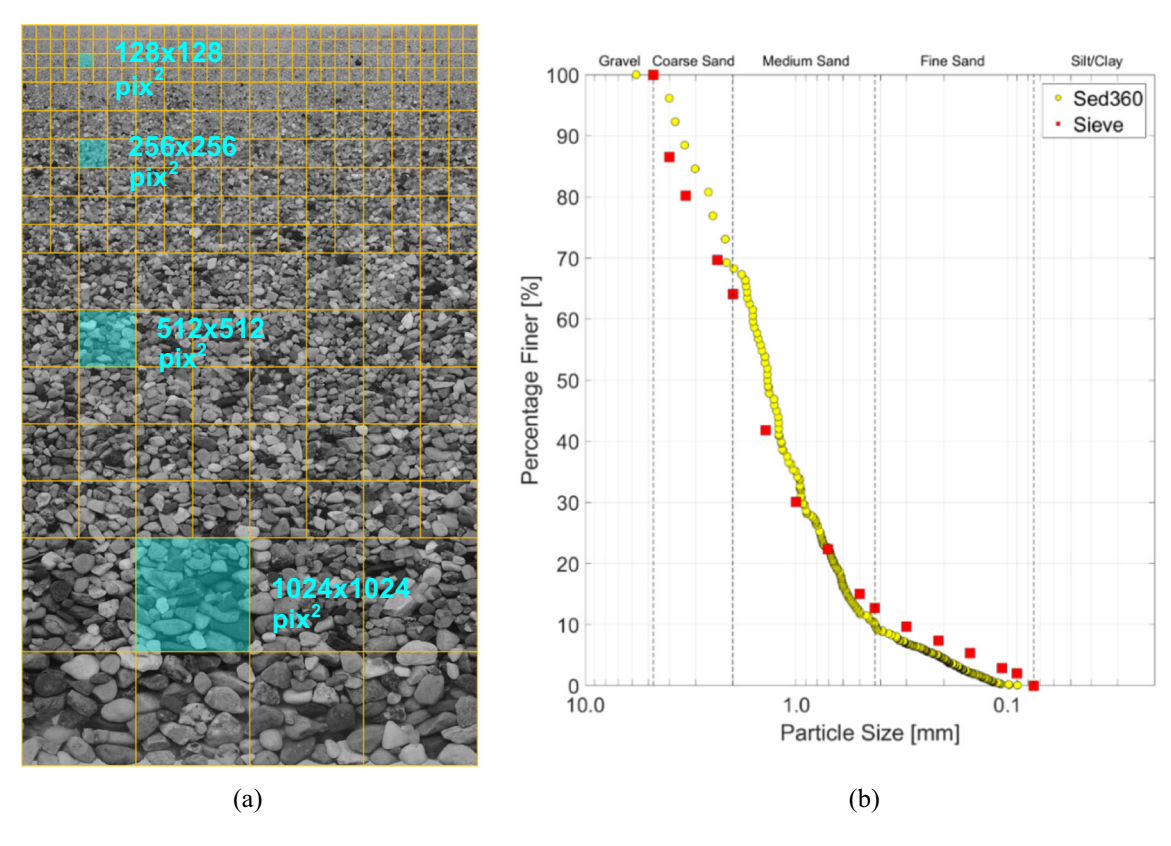


Fig. 14 Sed360 Results for Specimen C. a Autoadaptively determined analysis squares used to generate the HWT-based PSD, b PSD results

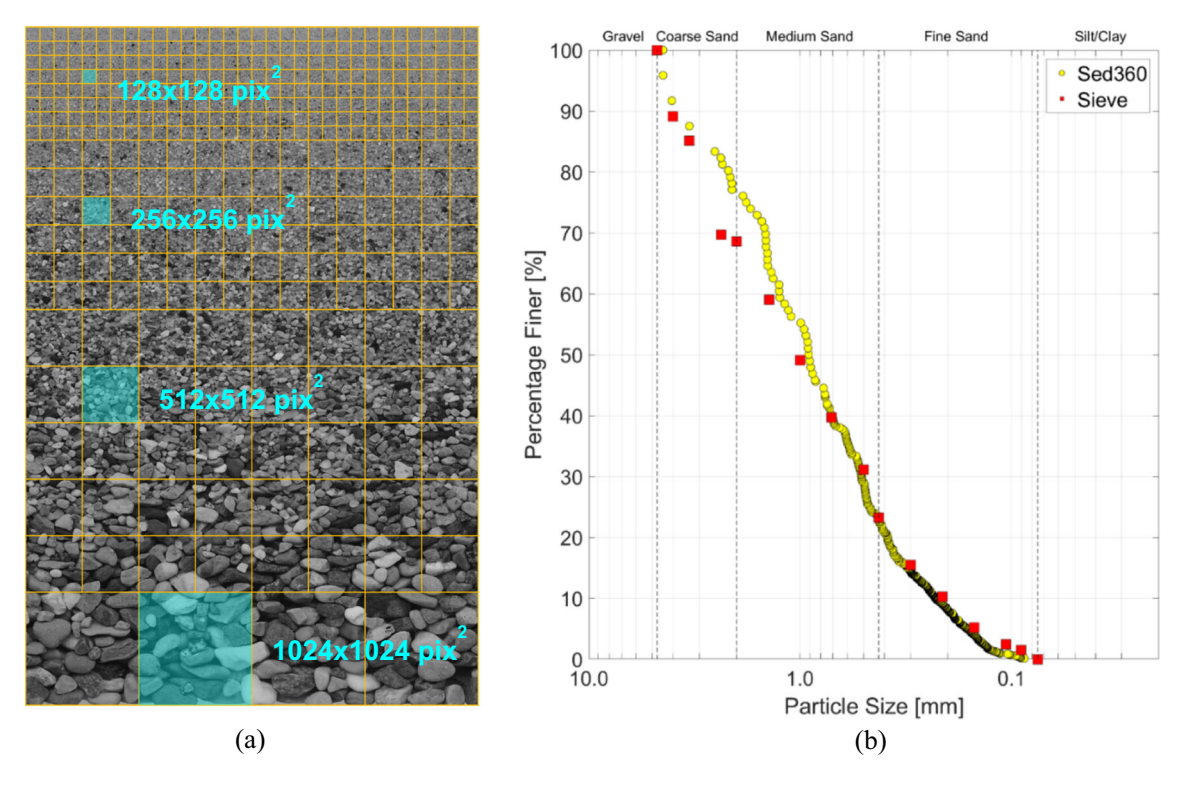


Fig. 15 Sed360 Results for Specimen D. a Autoadaptively determined analysis squares used to generate the HWT-based PSD, b PSD results



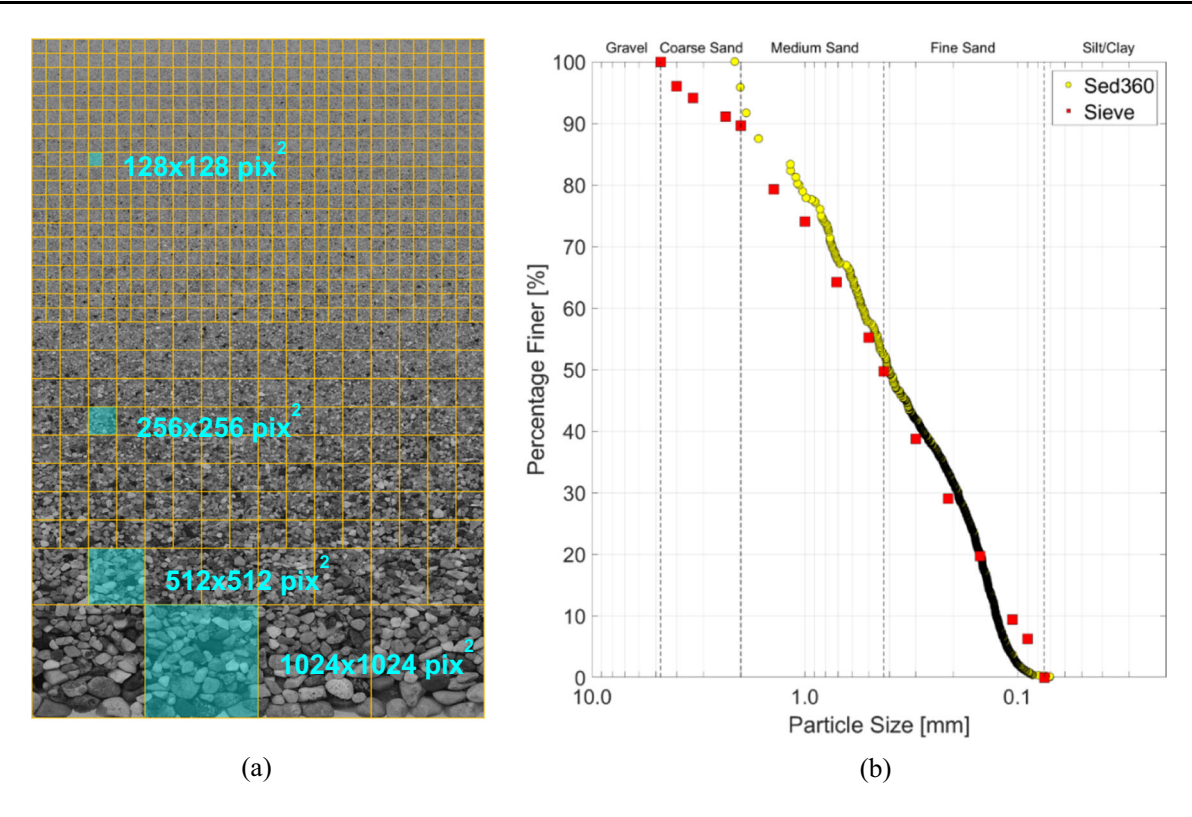


Fig. 16 Sed360 Results for Specimen E. a Autoadaptively determined analysis squares used to generate the HWT-based PSD, b PSD results

**Table 2** Details and results of the five sands tested in the Sed360

Item	Specimen A			Specimen B		Specimen C		Specimen D			Specimen E				
	Sed360		Sieve	Sed360		Sieve	Sed360		Sieve	Sed360		Sieve	Sed360		Sieve
	256 <sup>a</sup>	Auto <sup>b</sup>		256 <sup>a</sup>	Auto <sup>b</sup>		256 <sup>a</sup>	Auto <sup>b</sup>		256 <sup>a</sup>	Auto <sup>b</sup>		256 <sup>a</sup>	Autob	
Specimen size [g]	96.8			93.0			100.3			97.8			91.4		
Coarse sand [%]	2	44	67	1	35	50	2	31	37	1	24	31	0	8	10
Medium sand [%]	56	48	23	23	17	0	68	59	51	59	53	46	42	42	40
Fine sand [%]	42	8	10	76	48	50	30	10	12	40	23	23	58	50	50
$D_{60}$ [mm]	0.88	2.10	2.60	0.34	1.70	2.20	0.90	1.80	1.90	0.70	1.40	1.50	0.43	0.54	0.60
$D_{30}$ [mm]	0.36	1.40	1.80	0.23	0.23	0.23	0.42	0.96	1.00	0.38	0.50	0.50	0.21	0.20	0.21
$D_{IO}$ [mm]	0.31	0.45	0.40	0.16	0.13	0.10	0.31	0.43	0.30	0.24	0.22	0.21	0.14	0.12	0.10
$C_u^{\ c}$	2.8	4.7	6.5	2.1	13.1	22.0	2.9	4.2	6.3	2.9	6.4	7.1	3.1	4.5	6.0
${C_c}^{ m d}$	0.5	2.1	3.1	1.0	0.2	0.2	0.6	1.2	1.8	0.9	0.8	0.8	0.7	0.6	0.7

<sup>&</sup>lt;sup>a</sup>Using a fixed HWT analysis area size of 256 pixel by 256 pixel

present. Future research will address this relatively minor issue.

At the coarse end of the PSDs, the autoadaptive Sed360 method seems to undersize particles slightly. This is most evident and pronounced in Specimen E shown in Fig. 16. To understand why this occurs, Specimen E's row of  $1024 \times 1024$  pix<sup>2</sup> analysis squares in Fig. 16a is

examined. There are not enough coarse sand particles to fully fill up these four large analysis areas; the coarse sand particles fill only the bottom half of these  $1024 \times 1024$  pix<sup>2</sup> squares, while smaller sand particles fill the top half of this row. The HWT results for these analysis squares are like that in the Fig. 9 example. In both instances, for an analysis area that contains a range of particle sizes, the



<sup>&</sup>lt;sup>b</sup>Using the autoadaptive HWT analysis area sizing procedure from Fig. 10

<sup>&</sup>lt;sup>c</sup>Coefficient of Uniformity,  $C_u = D_{60}/D_{10}$ 

<sup>&</sup>lt;sup>d</sup>Coefficient of Curvature,  $C_c = (D_{30})^2/(D_{60} \times D_{10})$ 

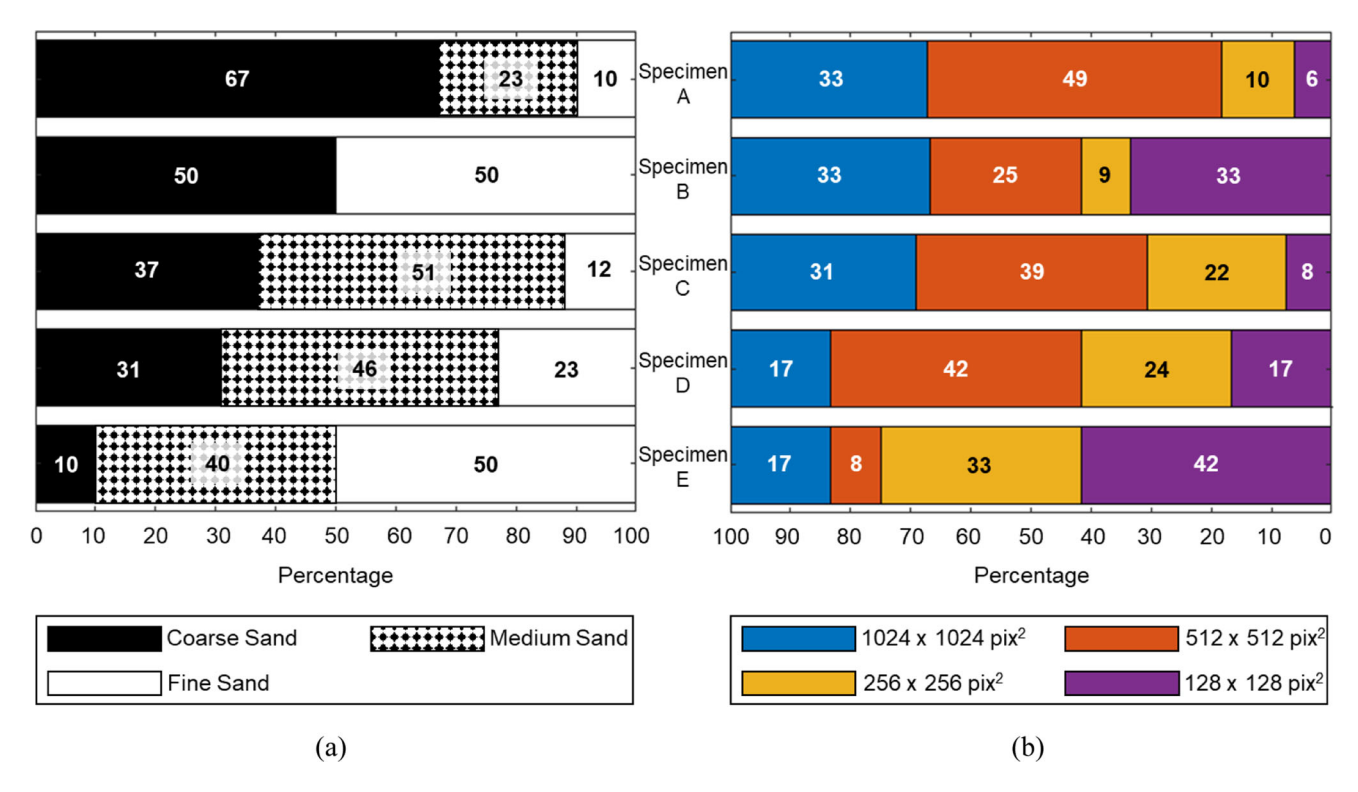


Fig. 17 Composition breakdown of the five specimens by percent. a Sand type percentages within each specimen according to sieve results, and b percentage of the specimen images (Figs. 12, 13, 14, 15, and 16) analyzed using each of the autoadaptively-selected HWT square sizes

HWT-determined particle size is smaller than the largest particles in the area, but larger than the finest particles. The possible solution to this in Fig. 9 was to quarter the larger analysis square. However using smaller squares for the coarse sand particles in Specimen E is not feasible (i.e. 50% of the row's energy curves would violate the rules of the autoadaptive HWT window sizing procedure), and ultimately the reason why the Sed360 PSD undersizes the coarse sand portion of the specimen. One solution to this problem is using a larger overall specimen size, but other remedies may exist that will be explored in the future.

### 6.2 Discussion of gap-graded sands

To explain why the Sed360 PSD reports 17% medium sand in the gap-graded Specimen B when the mix was created with only coarse and fine sand, the three rows of  $512 \times 512 \, \mathrm{pix}^2$  analysis squares in Fig. 13a are examined. These rows are located at the interface between the fine and coarse sand. In Fig. 18 the data points in the Sed360 PSD are color-coded to the analysis squares in these rows.

As expected, the analysis squares that appear to contain only fine sand (the green-colored squares in Fig. 18) yield particle size values (the green circle data points in Fig. 18) that fall within the fine sand range of the Sed360 PSD. Similarly, the analysis squares that appear to contain only coarse sand (pink squares) have particle sizes (pink circle

data points) that are within or very near the coarse sand range of the PSD.

The remaining areas in these three rows of analysis squares (the brown, cyan, and dark blue squares) correspond to the PSD data points that plot within the medium sand range. The three sets contain various proportions of fine and coarse sand. The brown areas contain mostly fine sand. Thus, the corresponding brown PSD data points lie at the finer end of the medium sand size range. The dark blue squares contain mostly coarse sand; thus, the dark blue Sed360 PSD data points lie in the coarser end of the medium size range. Lastly, the cyan areas are those that contain a more even mix of coarse and fine sand. As such, their points lie closer to the middle of the medium sand range. The HWT-based particle sizes for the brown, cyan, and dark blue analysis squares are essentially providing a weighted average for the varying amounts of coarse and fine sands in these areas. In doing so, the Sed360 PSD erroneously concludes that there is some medium-sized sand in Specimen B.

It is worth noting that Specimen B was intentionally engineered to test the limits of the Sed360 for a severely gap-graded sand. With particles between 2.0 and 0.425 mm entirely absent from this specimen, penetration of the pores in the coarse sand by fine sand particles was guaranteed. A naturally-occurring gap-graded sand would typically not have such a wide range of particles sizes missing entirely.



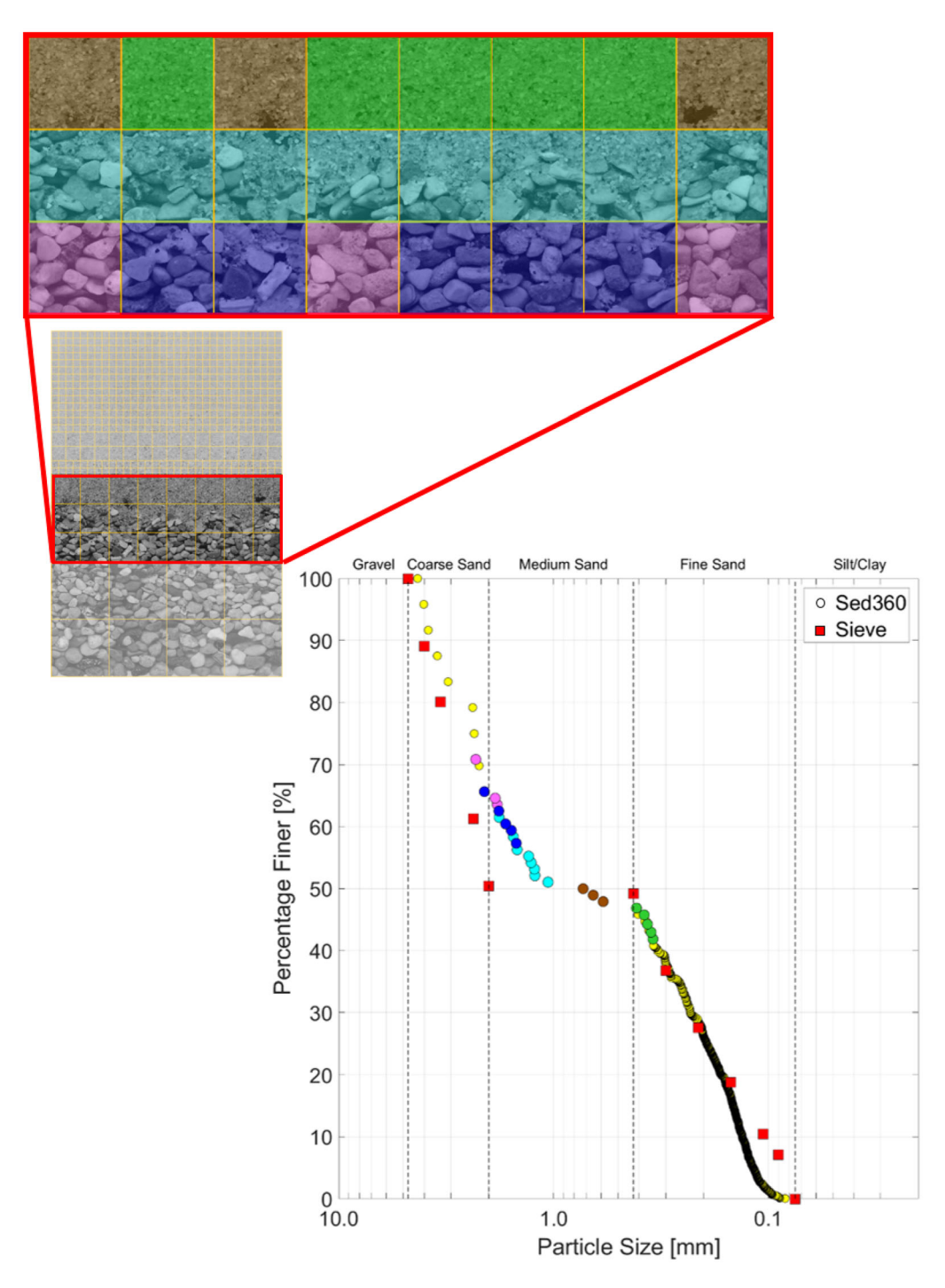


Fig. 18 Investigating the HWT analysis squares at the coarse and fine sand interface in Specimen B

Even small amounts of medium-sized particles would create a sand filter that would limit the pore "clogging". Better agreement should therefore be expected between the Sed360 and sieve PSDs for naturally-occurring gap-graded sands.

### 7 Conclusions

The hardware developments of the Sed360 afforded the expansion of testable soils by SedImaging to include the entire sand range according to the Unified Soil Classification System (4.75 to 0.075 mm; No. 4 sieve to No. 200



sieve). The expansion of testable soils necessitated a reexamination of the existing HWT-based image analysis method used to generate the PSDs of soil tested by SedI-maging. In doing so, the calibration equation used in the method has been updated. More significantly, a new method has been created that autoadaptively adjusts the size of the HWT analysis areas to more accurately determine particle size distributions for the expanded range of particle sizes. Five specimens of sand with varying gradations and amounts of coarse, medium, and fine sand were tested and analyzed using the new autoadaptive HWT-based image analysis method. Strong agreement between the Sed360 and sieve results was observed when the variable window sizes were used.

Acknowledgements This material is based upon work supported by the US National Science Foundation under Grant CMMI 1825189. ConeTec Investigations Ltd. and the ConeTec Education Foundation are acknowledged for their support to the Geotechnical Engineering Laboratories at the University of Michigan. The authors thank Steve Donajkowski for providing design suggestions and machining for the Sed360.

**Data Availability** The datasets generated during and/or analyzed during the current study are available from the corresponding author on reasonable request.

### References

- ASTM International (2019) Standard test method for sieve analysis of fine and coarse aggregates. ASTM C136/C136M-19, West Conshohocken, PA: ASTM International, approved December 1, 2019. https://doi.org/10.1520/C0136\_C0136M-19
- Cabrera-Navarrete E, Ronquillo-Jarillo G, Markov A (2020) Wavelet analysis for spectral inversion of seismic reflection data. J Appl Geophys 177:104034. https://doi.org/10.1016/j.jappgeo. 2020.104034
- 3. Chatterjee P (2015) Wavelet analysis in civil engineering, 1st edn. CRC Press, Boca Raton
- Ching J, Wang J-S, Juang CH, Ku C-S (2015) Cone penetration test (CPT)-based stratigraphic profiling using the wavelet transform modulus maxima method. Canadian Geotech J 52(12):1993–2007. https://doi.org/10.1139/cgi-2015-0027
- Ding L, Ma L, Luo H, Yu M, Wu X (2011) Wavelet analysis for tunneling-induced ground settlement based on a stochastic model. Tunnel Underground Space Tech 26(5):619–628. https://doi.org/ 10.1016/j.tust.2011.03.005
- Haar A (1910) Zur Theorie der Orthogonalen Functionensysteme. Math Ann 69(3):331–371
- Hryciw RD, Ohm H-S, Zhou J (2015) Theoretical basis for optical granulometry by wavelet transformation. J Comput Civ Eng 29(3):04014050. https://doi.org/10.1061/(ASCE)CP.1943-5487.0000345
- Hryciw RD, Jung Y (2008) Accounting for void ratio variation in determination of grain size distribution by soil column image processing. In: Proceedings, GeoCongress 2008, ASCE, Reston, VA, 966–973. https://doi.org/10.1061/40972(311)121
- Hryciw RD, Jung Y, Susila E, Ibrahim A (2009) Thin soil layer detection by VisCPT and FEM simulations. In: Proceedings 17th international conference on soil mechanics and geotechnical

- engineering (ICSMGE), IOS, Amsterdam, Netherlands, pp. 1052–1055
- Michigan Department of Transportation (MDOT) (2010) Materials Source Guide. 902, Lansing, MI
- Mollaioli F, Bosi A (2011) Wavelet analysis for the characterization of forward-directivity pulse-like ground motions on energy basis. Meccanica 47(1):203–219. https://doi.org/10.1007/s11012-011-9433-1
- 12. Nievergelt Y (1999) Wavelets made easy. Birkhäuser, Boston
- Ohkami T, Nagao J, Koyama S (2006) Identification of elastic materials using wavelet transform. Comput Struct 84(29):1866–1873. https://doi.org/10.1016/j.compstruc.2006.08. 030
- Ohm H-S, Hryciw RD (2014) Size distribution of coarse-grained soil by SedImaging. J Geotech Geoenviron Eng 140(4):04013053. https://doi.org/10.1061/(ASCE)GT.1943-5606. 0001075
- Ohm H-S, Sahadewa A, Hryciw RD, Zekkos D, Brant N (2013) Sustainable soil particle size characterization through image analysis. Geotechn Geol Engr 31:1647–1652. https://doi.org/10. 1007/s10706-013-9657-z
- Pang Y, Wang N, Wang K, Liu Z, Nie L, Xu X (2020) Multiscale constrained inversion method for direct current resistivity tomography based on Haar wavelet transform. Inst Electr Electron Eng Access 8:170195–170202. https://doi.org/10.1109/ ACCESS.2020.3024286
- 17. Prokoph A, Patterson RT (2004) From depth scale to time scale: transforming sediment image color data into a high-resolution time series. In: Francus P (ed) Developments in Paleoenvironmental Research 7: Image Analysis, Sediments and Paleoenvironments. Kulwer Academic Publishers, Dordrecht, pp 143–164
- Shin S, Hryciw RD (2004) Wavelet analysis of soil mass images for particle size determination. ASCE J Comput Civil Eng 18(1):19–27. https://doi.org/10.1061/(ASCE)0887-3801(2004)18:1(19)
- Sudarsan B, Ji W, Adamchuk V, Biswas A (2018) Characterizing soil particle sizes using wavelet analysis of microscope images. Comput Elect Agriculture 148:217–225. https://doi.org/10.1016/j. compag.2018.03.019
- Sun Y, Xiao Y, Hanif KF (2015) Compressibility dependence on grain size distribution and relative density in sands. Sci China Tech Sci 58:443–448. https://doi.org/10.1007/s11431-015-5768-5
- Vassiliou M, Makris N (2011) Estimating time scales and length scales in pulselike earthquake acceleration records with wavelet analysis. Bull Seismol Soc Am 101(2):596–618. https://doi.org/ 10.1785/0120090387
- Ventola A, Horstmeier G, Hryciw RD, Kempf C, Eykholt J (2020) Particle size distribution of kalamazoo river sediments by FieldSed. J Geotech Geoenviron Eng 146(12):05020012. https://doi.org/10.1061/(ASCE)GT.1943-5606.0002421
- Ventola A, Hryciw RD (2023) The Sed360 test for rapid sand particle size distribution determination. ASTM Int Geotechn Testing J. https://doi.org/10.1520/GTJ20220032
- 24. Ventola A, Hryciw RD (2019) On-site particle size distribution by FieldSed. In Geo-Congress: Engineering Geology, Site Characterization, and Geophysics, edited by C. Meehan, S. Kumar, M. Pando, and J. Coe, 143–151. Reston, VA: ASCE. https://doi.org/10.1061/9780784482131.015
- Xiao Y, Long L, Evans TM, Zhou H, Liu H, Stuedlein AW (2019) Effect of particle shape on stress-dilatancy responses of medium-dense sands. J Geotech Geoenviron Eng 145(2):04018105. https://doi.org/10.1061/(ASCE)GT.1943-5606. 0001994
- Xiao Y, Zhao C, Sun Y, Wang S, Wu H, Chen H (2021) Compression behavior of MICP-treated sand with various gradations.



Acta Geotech 16:1391–1400. https://doi.org/10.1007/s11440-020-01116-2

**Publisher's Note** Springer Nature remains neutral with regard to jurisdictional claims in published maps and institutional affiliations.

Springer Nature or its licensor (e.g. a society or other partner) holds exclusive rights to this article under a publishing agreement with the author(s) or other rightsholder(s); author self-archiving of the accepted manuscript version of this article is solely governed by the terms of such publishing agreement and applicable law.

